Sessile super-droplets as quasi-static wall deformations in direct numerical simulation of turbulent channel flow

Philipp Bahavar[a,b], Claus Wagner[a,b]

[a]*German Aerospace Center (DLR), Bunsenstr. 10, Göttingen, 37073, Germany*
[b]*Technische Universität Ilmenau, Helmholtzring 1, Ilmenau, 98693, Germany*

Abstract

Condensation is an important aspect of many flow applications due to the ubiquitous presence of humidity in the air at ambient conditions. For direct numerical simulations of such flows, simulating the gas phase as a mixture characterized by temperature and humidity coupled by the latent heat release and absorption has been shown to yield results consistent with multiphase direct numerical simulations at reduced cost. In the case of surface condensation, the deposition of condensate droplets represents an additional mechanism for flow modification. Extending the single-phase approach by tracking the mean deposition rates and consolidating the condensate mass into static super-droplets reintroduces the effects of surface droplets on the flow while retaining the computational advantages of simulating only the gas phase. Results of simulations of turbulent flow through a cooled, vertical channel with and without such droplets illustrate the additional effects captured compared to the original approach. In the immediate vicinity of a super-droplet, turbulent heat and vapor transport towards the cooled wall is enhanced. Direct impingement and deflection of the flow on the super-droplet cause a qualitative change in the distribution of the condensation rates, increasing on the surface of the super-droplets and decreasing in the surrounding regions. This modification of the wall-near transport leads to increased global cooling and drying efficiency compared to a smooth channel.

Keywords: Direct numerical simulation, Condensation, Channel flow, Heat transfer

1. Introduction

Fluid flows with condensable components are relevant to a wide variety of applications, from the design of heat exchangers to the formation of clouds in the atmosphere.

The ubiquity of ambient humidity in the air means that condensation can occur in any space where humid air is exposed to sufficient temperature differences. This condensation can cause problems, such as for example the fogging of the windshield in a car, where the warm air in the heated interior meets the cool surface. The energy required to defog the windshield is considerable. This is especially true for electric vehicles, which cannot easily use the waste heat from the engine (Lorenz, 2015).

The combination of thermodynamic and fluid mechanical effects and phenomena presents a challenge when trying to model flows with phase transitions due to the variety of interactions and the broad range of length and time scales involved. For application-oriented research, models based on the relative humidity and average mass transfer rates are applied to Reynolds-averaged Navier–Stokes (RANS) simulations, which provide large-scale results for condensation and evaporation on surfaces (Leriche et al., 2015).

For the investigation of fundamental mechanisms and interactions between flow and phase transitions, fully resolved direct numerical simulations (DNS) employ a spectrum of techniques for the computation of multiphase flows and phase transitions in such flows. They range from approaches with inert ideal tracer particles, one-way or two-way coupling between the fluid and the particles by means of drag, four-way coupling with the additional inclusion of particle-particle collisions, to methods with fully resolved interfaces and internal dynamics. For an overview, see e.g. reviews by Balachandar and Eaton (2010) or Kuerten (2016). In general, the high cost of multiphase DNS tends to limit the investigations to generic geometries (Russo et al., 2014) or individual droplets (Orazzo and Tanguy, 2019).

For flows at ambient conditions, where vapor loads and temperature differences are limited compared to engineering applications, condensation is almost exclusively confined to the cooled surfaces themselves, with only negligible condensation within the volume and consequently negligible droplet volume fraction. In this case, using a single-phase DNS of a homogeneous mixture of dry air and water vapor and modeling phase transition effects with sources and sinks for the vapor concentration and associated latent heat yields reliable results, as validated against two-way coupled multiphase DNS (Bahavar and Wagner, 2020). In addition to the coupling between latent heat of condensation and vapor concentration, effects due to temperature, vapor concentration, and thermal and solutal buoyancy are considered here.

The concentration of condensation on surfaces highlights the need to consider condensate droplets and their effect on the turbulent transport processes. However, an extension of the the original approach should preserve the single-phase nature of the simulation and the associated computational advantages.

Email address: philipp.bahavar@dlr.de (Philipp Bahavar)

In meteorological simulations, the super-droplet method (Shima et al., 2009) is used to address the problem of divergent length scales between droplets and flow and the associated computational challenge. These synthetic droplets preserve selected physical quantities of the original pattern while reducing the resolution requirements to those inherent to the flow simulation. Adapting the concept of super-droplets to sessile condensate droplets on a cooled surface allows DNS of turbulent flow with condensation without having to resolve droplets much smaller than the Kolmogorov scale.

Using the fact that adhesive forces limit the mobility of sessile droplets, the super-droplets are then assumed to be static surface deformations which interact with and influence the flow. The interaction between droplets and flow mirrors a one-way coupling of fluid and particles, where the particle motion is governed by the fluid flow. Here, the direction of the interaction is reversed, with the droplets influencing the flow fields, but remaining unaffected by the flow.

The accuracy of the single-phase DNS coupled with the comparatively lower computational cost for the inclusion of phase transitions involving sessile condensate droplets makes this approach well suited for the study of the interaction between condensation and turbulent flow, which requires a comparatively large flow domain (Jiménez and Moin, 1991).

This article presents the application of the extended approach to the turbulent flow of humid air through a cooled, vertical channel geometry, with flow parameters chosen to represent conditions relevant to vehicle or cabin ventilation.

2. Governing equations

The approach to the treatment of condensation in the context of vehicle ventilation takes advantage of the specific thermodynamic parameters of this application. Humid air is described as a homogenous fluid consisting of a carrier phase of dry air in which water vapor is dissolved (Bahavar and Wagner, 2020). The dynamics of this fluid with density ρ and kinematic viscosity ν are described by the Navier–Stokes equations for incompressible flow of a fluid with constant properties,

$$\nabla \cdot \mathbf{u} = 0, \tag{1}$$

$$\frac{\partial \mathbf{u}}{\partial t} + (\mathbf{u} \cdot \nabla)\mathbf{u} = -\frac{1}{\rho}\nabla p + \nu \nabla^2 \mathbf{u} + \mathbf{f}, \tag{2}$$

where eq. (1) provides the continuity condition and eq. (2) the evolution of the velocity $\mathbf{u}$ experiencing a pressure gradient ∇p and a general body force $\mathbf{f}$.

Both the temperature T and the humidity in the form of the molar vapor concentration c of the humid air are described by convection-diffusion equations with general source terms S,

$$\frac{\partial T}{\partial t} + (\mathbf{u} \cdot \nabla)T = \kappa \nabla^2 T + S_T, \tag{3}$$

$$\frac{\partial c}{\partial t} + (\mathbf{u} \cdot \nabla)c = D \nabla^2 c + S_c, \tag{4}$$

with thermal diffusivity κ and the binary mass diffusion coefficient D.

The presence of temperature and humidity gives rise to thermal and solutal buoyancy $\mathbf{B}_T$ and $\mathbf{B}_c$, respectively (Hammou et al., 2004). For the ranges considered here, the Boussinesq approximation applies (Gray and Giorgini, 1976)) and the linearized buoyancy forces are

$$\mathbf{B}_T = -\beta_T (T - T_{ref})\mathbf{g} \tag{5}$$

$$\mathbf{B}_c = -\beta_c (c - c_{ref})\mathbf{g} \tag{6}$$

with the gravitational acceleration $\mathbf{g}$. The expansion coefficients with respect to temperature and concentration are

$$\beta_T = \frac{1}{\rho}\frac{\partial \rho}{\partial T}\bigg|_{T_{ref}}, \quad \beta_c = \frac{1}{\rho}\frac{\partial \rho}{\partial c}\bigg|_{c_{ref}}. \tag{7}$$

Setting the force in eq. 2 equal to

$$\mathbf{f} = \mathbf{B}_T + \mathbf{B}_c \tag{8}$$

includes the buoyancy contributions in the velocity equation. Thus, temperature and vapor concentration act as active scalars in this framework, coupled to the velocity field via buoyancy and in turn affected by the convective transport with the flow.

For the calculation of the phase change, the effect of the condensation on the gas phase is considered first. The source term S_c in eq. (4) expresses the loss or gain of vapor concentration in a volume V due to condensation or evaporation over a surface A. Using the ideal gas law as the equation of state and the Hertz–Knudsen–Schrage equation (Marek and Straub, 2001), the vapor source term is

$$S_c = -\frac{2\sigma_c}{2 - \sigma_c}\frac{A}{V}\sqrt{\frac{RT}{2\pi M}}(c - c_{sat}). \tag{9}$$

Here σ_c is the condensation coefficient, which expresses the probability that a vapor molecule remains in the liquid phase after condensation, and is assumed in this formulation to be equal to the similarly defined evaporation coefficient σ_e. The condensation rate is proportional to the difference between the current vapor concentration and the saturation value c_{sat}. This saturation concentration is itself a function of the temperature, described for example by the Magnus formula (Alduchov and Eskridge, 1996).

Conversely, the temperature source term S_T in eq. (3) captures the effect of heating or cooling due to the release or absorption of latent heat during the phase transition,

$$S_T = -\frac{h_v}{c_p} S_c, \tag{10}$$

with the ratio of the latent heat of vaporization h_v and the specific heat capacity of the fluid c_p as the proportionality constant relating the temperature source to the vapor source. This connection between temperature and concentration completes the full coupling between the two scalar fields and the velocity.

The treatment of liquid water resulting from condensation is separate for liquid inside the volume and on cooled surfaces. With the low total vapor concentrations and limited subcooling encountered in vehicle ventilation, the amount of condensate

formed inside the volume is negligible. Consequently, it is ignored in this approach and no transport of liquid water with the airflow in the form of droplets is simulated.

Instead, condensation occurs predominantly on cooled surfaces. In wall-bounded flows, droplets forming on these walls have the potential to significantly affect the flow throughout the whole geometry. This surface modification provides an additional mechanism for condensation to affect such flows.

Condensate mass accumulates at the surface at the same rate as it is removed from the fluid by condensation, expressed by the source term S_c in eq. (9). This accumulation leads to a changed surface shape on the one hand, and to a momentum source due to the motion of the liquid-gas interface on the other hand. A comparison between the total vapor flux through the channel and the condensation flux shows that the latter effect is negligible as follows.

In the upper limit of complete condensation of all available vapor, the mass flux across the phase boundary ϕ_{PT} is equal to the vapor mass flux convected by the fluid

$$\phi_c = c\rho_v u_b, \tag{11}$$

where u_b is the convection velocity and ρ_v the density of pure vapor. Assuming that the condensate grows as a uniform film over a cooled surface, the film thickness grows with velocity

$$u_f = \phi_{PT}\,\frac{1}{\rho_l} \leq \frac{c\rho_v}{\rho_l}\,u_b. \tag{12}$$

Since the ratio between the vapor density ρ_v and the liquid density ρ_l is very small (on the order of 10^{-3}), and the vapor concentration c at ambient conditions is also small ($\simeq 10^{-2}$), the theoretical film growth velocity u_f is negligible compared to the convection u_b (Tryggvason et al., 2005). Consequently, the momentum transfer at the liquid-gas interface is negligible, and the interface is effectively static with respect to the flow.

The microscopic mechanisms of nucleation, which require simulations at the molecular level (Niu and Tang, 2018), and the simultaneous isolated droplet growth and droplet coalescence (Medici et al., 2014), which span length and time scales orders of magnitude beyond those of the turbulent flow, preclude a fully resolved simulation of the full dynamics. At the same time, only the largest droplets penetrating through the viscous sublayer cause a direct change in the turbulent flow, while smaller droplets leave the first and second order statistical moments largely unchanged (Chan-Braun et al., 2011).

The slow growth of the condensate precludes fully resolved simulations on the timescales necessary to achieve appreciable droplet sizes. Instead, a pattern of synthetic droplets is generated based on a target droplet diameter D' that determines the size distribution of the resulting droplets. The generation process is as follows.

A coarser supplementary grid with spacing of the order of D' is applied to the surface on top of the computational grid. Within each grid cell, the average condensation rate is determined over a sufficiently long time to represent the long-term droplet growth conditions. Multiplying the average condensation rate $\langle\phi_{PT}\rangle$ by an arbitrary growth time t_g then gives the total available condensate mass. By idealizing the droplet shapes as hemispheres, the droplet radii R_i are directly related to their mass m_i. Choosing now t_g so that the extrapolated mass over the cooled surface corresponds to the desired mean droplet size $\langle R\rangle$ and applying the extrapolation for each cell i separately as

$$m_i = \langle\phi_{PT}\rangle_i\, t_g \tag{13}$$

results in synthetic droplets that consolidate all available condensate mass within their respective grid cell. This procedure retains the underlying information about the inhomogeneity of local condensation rates provided by the original simulation by conserving the condensate mass on the supplementary grid. The resulting droplets have radii of the order of the target value, but vary in size based on the available mass. To avoid artificial regularity introduced by the grid, the synthetic droplets are randomly placed within their grid cell. Figure 1 provides an illustration of the droplet generation process.

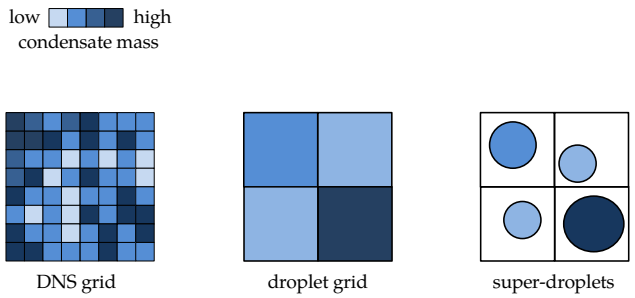

Figure 1: Illustration of droplet pattern formation. Condensate masses extrapolated from the surface cells of the DNS (left) are accumulated in cells of sizes on the order of the droplet radii (center), and then combined into droplets with volumes corresponding to the available mass (right), thus conserving mass at the grid level.

Since the presence of droplets changes the flow over the surface, the average condensation rate is also affected. Accordingly, the growth time t_g must be short enough that the majority of the skipped growth dynamics are still governed by the initial values for the average condensation, but long enough to provide a sufficiently robust average value.

Due to the effectively static nature of the droplets, this investigation focuses on their influence on the flow via the modification of the cooled surface. For a Reynolds number of $Re = 2000$ and subcooling on the order of 10 K, the minimum size for a thermodynamically viable droplet is five orders of magnitude smaller than the Kolmogorov scale. Consequently, the vast majority of the droplets are far smaller than the smallest scales of the turbulent flow (Kim and Kim, 2011). Restricting the investigation to only the largest droplets using the approach outlined above avoids the necessity to resolve droplets over all scales of the self-similar growth process. The droplets are modeled as solid, hemispherical wall deformations, ignoring their internal

properties, such as the effect of curved liquid interfaces on the saturation pressure or the existence of a temperature gradient within a droplet (Rose, 2002). This approach isolates the direct geometric effect of the droplets on the flow and subsequently on the heat and vapor transport, without confounding thermodynamic effects.

3. Simulation setup

The governing equations are solved with a finite volume method, which is partly based on the library of the open source finite volume method OpenFOAM (The OpenFOAM Foundation), adapted to the requirements of Direct Numerical Simulations.

To choose an approach suitable for DNS of turbulent channel flows, three different combinations of discretization schemes have been tested in the past (Kath and Wagner, 2016). In the first combination, a second order central difference scheme was used for the spatial discretization together with a second order implicit backward time integration method and the so-called PISO algorithm (Issa, 1986), which is the pressure-velocity coupling recommended by OpenFoam for thermally driven flows. In the second combination, the second order accurate central difference scheme was used together with an explicit second order accurate Euler-leapfrog time integration scheme (Wagner, 1996) and a projection method first introduced by Chorin (1968) and Témam (1969) for coupling the pressure and velocity fields. The third combination was similar to the second, except that fourth-order accurate central differences were used for the spatial discretization. By comparing the results obtained with these three combinations with those of the spectral DNS of Kasagi and Nishimura (1997) it was shown that the combination of second or fourth order accurate spatial discretization, explicit Euler-leapfrog time integration and the projection method gives the best agreement for the velocity and temperature fields.

The leapfrog integration step for the velocity field is given by

$$\mathbf{u}^*_{t+1} = \mathbf{u}_{t-1} + 2\Delta t \left(D_{t-1} + C_t + P_t\right), \tag{14}$$

with a time-lagged diffusion term D_{t-1} (Manhart, 2004), convection term C_t, global pressure gradient P_t, and time step Δt. An averaging step

$$\mathbf{u}^*_{t+1} = \frac{1}{2}\left(\mathbf{u}_{t-1} + \mathbf{u}_t\right) + \frac{3}{2}\left(D_{t-1} + C_t + P_t\right) \tag{15}$$

is introduced every 50 iterations to avoid unphysical oscillations.

Similarly, the leapfrog integration step for the temperature field is

$$T_{t+1} = T_{t-1} + 2\Delta t \left(D_{T,t-1} + C_{T,t} + S_{T,t}\right), \tag{16}$$

with the diffusion term D_T, the convection term C_T and the source term S_T from eq. (3). Treatment of the concentration field is fully analogous.

The time step of the integration is limited by the stability of the explicit scheme. The stability criterion for the leapfrog scheme in a convection-diffusion problem as derived by Shishkina and Wagner (2004) can be extended to include thermal and mass diffusion in addition to momentum diffusion,

$$\Delta t \leq \left(\sum_i \frac{u_b}{\Delta x_i} + \sum_i \frac{4\Gamma}{\Delta x_i^2} \right)^{-1}. \tag{17}$$

Here, Δx_i is the mesh spacing along each of the three axes, and $\Gamma = \max(\nu, \kappa, D)$ is the largest relevant diffusion coefficient.

The projection method couples pressure and velocity for the incompressible flow by solving the Poisson equation for the pressure,

$$\nabla^2 p = \frac{\rho}{\Delta t} \nabla \cdot \mathbf{u}^*_{t+1} \tag{18}$$

and correcting the initial guess for the updated velocity $\mathbf{u}^*_{t+1}$, ensuring a divergence-free field $\mathbf{u}_{t+1}$. Second order accurate central differences are used for the spatial discretization, as the marginal additional accuracy of a fourth order scheme introduces disproportionate complexity compared to the second order scheme. (Kath and Wagner, 2016).

The investigated geometry is a channel with half-width δ and overall dimensions $6\pi\delta \times 2\delta \times 2\pi\delta$. It is oriented vertically, with flow from top to bottom along the direction of gravity. At both ends, the boundaries create an inlet-outlet configuration, while periodic boundaries apply in the spanwise direction.

Humid air at ambient conditions is chosen as the working fluid, with Prandtl number $Pr = \nu/\kappa = 0.73$ and Schmidt number $Sc = \nu/D = 0.65$.

The temperature T_{in} and the vapor concentration c_{in} at the inlet are chosen such that the air is undersaturated, $c_{in} < c_{sat}(T_{in})$. Expressed with the dew point temperature, this is equivalent to $T_{dp}(c_{in}) < T_{in}$. One of the channel walls is adiabatic, while the opposite wall is cooled to $T_c = T_{in} - \Delta T$. This wall temperature is such that the subcooling with respect to the inlet vapor concentration is $T_{dp}(c_{in}) - T_c = 0.38\Delta T$, allowing condensation to occur. The concentration at the cooled wall evolves freely and is completely determined by the temperature, resulting in a lower bound of $c_{sat}(T_c)$.

The thermal Grashof number quantifies the buoyancy due to the temperature difference $\Delta T = T_{in} - T_c$,

$$Gr_T = \frac{g\beta_T \Delta T \delta^3}{\nu^2} = 38\,000. \tag{19}$$

Analogously, the solutal Grashof number is determined by $\Delta c = c_{in} - c_{sat}(T_c)$,

$$Gr_c = \frac{g\beta_c \Delta c \delta^3}{\nu^2} = 1500. \tag{20}$$

Both buoyancy contributions act in the same direction. A decrease in temperature leads to a downward force, as does a decrease in vapor concentration. Together with a bulk velocity u_b, resulting in bulk and friction Reynolds numbers

$$Re = \frac{u_b \delta}{\nu} = 2000, \quad Re_\tau = \frac{u_\tau \delta}{\nu} = 135, \tag{21}$$

the balance between natural and forced convection is expressed via the Richardson number,

$$Ri = \frac{Gr_T + Gr_c}{Re^2} = 0.01. \tag{22}$$

Finally, the Jakob number $Ja = \Delta T c_p / h_v = 0.012$ gives the ratio between sensible and latent heat in the coupling between temperature and concentration via the phase transition.

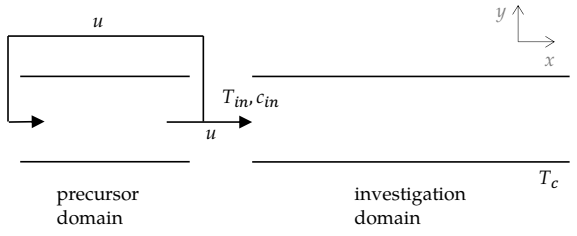

Figure 2: A schematic overview of the coupled simulation setup, consisting of a cyclic precursor domain generating isothermal, turbulent flow, and the investigation domain in an inlet-outlet configuration with a cooled wall.

To investigate fully developed turbulent flow consistent with the desired Reynolds number along the entire length of the channel, the velocity inlet conditions are provided by an auxiliary domain (Wagner, 1996). It consists of a biperiodic channel with dimensions $4\pi\delta \times 2\delta \times 2\pi\delta$, matching the wall distance and width of the primary channel. Inside this channel, an isothermal turbulent flow with bulk velocity u_b is continuously simulated. At the cyclic outlet, the velocity field is mapped back to the inlet, but also fed forward to the inlet boundary of the investigation domain, where the temperature and concentration boundary conditions are applied (Bellec et al., 2017). In this way, the generation domain serves as an infinite-length inflow channel, allowing all turbulence statistics to fully develop before entering the investigation domain. Figure 2 gives a schematic overview of this setup.

The pressure boundaries complement the velocity boundaries, with a zero-gradient condition at the inlet and fixed pressure at the outlet, corresponding to the zero-gradient outlet condition applied to the velocity.

To meet the resolution requirements of the DNS, the channel is discretized into $480 \times 180 \times 316$ hexahedral cells. The distribution is uniform along the streamwise and spanwise directions, resulting in a resolution of $\Delta x^+ = 5.3$ and $\Delta z^+ = 2.7$, respectively. In the wall-normal direction, the resolution is increased, with 15 grid points within the viscous sublayer at the channel walls to adequately capture the high gradients present here. Using a hyperbolic tangent distribution, the resolution varies between $\Delta y^+ = 0.2 - 3.2$, with maximum resolution directly at the walls and minimum resolution in the center of the channel.

In the generation domain, the mesh resolution is identical, resulting in $320 \times 180 \times 316$ cells. Exact matching of the meshes of both domains avoids numerical artifacts at the boundary.

The simulation is initialized by computing isothermal flow at the prescribed Reynolds number until statistically steady turbulence is established in both domains. Then the calculations for the evolution of the temperature (3) and the vapor concentration (4) are included. The simulation then continues until a statistically steady state is reached, accounting for influence of the added scalar fields. In this configuration, data are then collected over an interval $T = 30\,\delta/u_\tau = 30\,t^+$ both to obtain the average condensation rates needed to generate the droplet pattern as well as to serve as a baseline for the following simulation including these droplets.

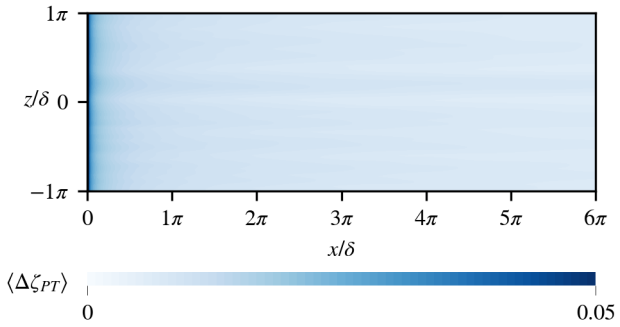

Figure 3: The distribution of the average condensation rate at the cooled wall of the smooth channel. Very high rates are found directly at the inlet. Condensation decreases along the channel, and a spanwise variation can be observed.

Figure 3 shows this average condensation rate directly at the cooled wall expressed in terms of the dimensionless concentration,

$$\zeta = \frac{c - c_{sat}(T_c)}{\Delta c}, \tag{23}$$

Condensation intensity is inhomogeneous over the surface. Condensation rates are highest directly at the inlet of the channel, where the fluid carrying the full vapor load first encounters the cooled wall. As the streamwise position increases, the progressive drying of the fluid from upstream condensation reduces the driving force for further condensation, and the rates decrease accordingly. This streamwise evolution is combined with a periodic spanwise variation that shows the effect of the structure of the turbulent flow on the convective transport of vapor to the wall.

The pattern of synthetic super-droplets is then generated based on these time-averaged condensation rates, while preserving the information about the streamwise and spanwise variation of the condensation intensity. To best illustrate the extended single-phase approach with static sessile droplets, the extrapolated growth time t_g is chosen such that even the smallest super-droplets reach a height of $h^+ = 5$, thereby ensuring that the majority of the droplets penetrate the viscous sublayer and interact directly with the turbulent flow.

The resulting pattern consists of $N = 1900$ spherical caps with an average height of $\langle h^+ \rangle_N = 6.4$ and an average footprint radius $\langle R \rangle_N = 8.9$. Figure 4 gives an overview of the pattern and the distribution of the droplet sizes on the cooled wall. Consistent with the underlying condensation rates, super-droplets are

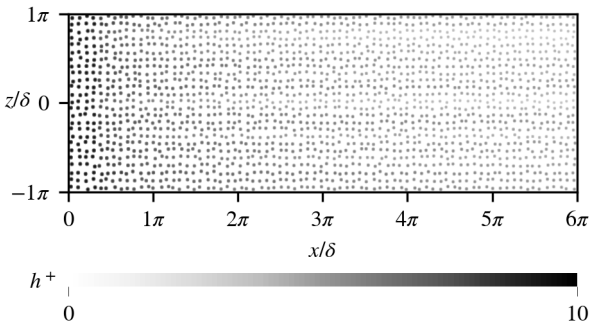

Figure 4: The super-droplet pattern placed on the cooled wall, with different heights and footprints ensures local conservation of condensate mass.

larger near the inlet, with sizes decreasing along the streamwise direction. Droplet volumes are adjusted by reducing the droplet height and footprint while keeping the radius of curvature constant. For the largest super-droplets, this results in perfect hemispheres with $h^+_{max} = R^+_{max} = 9.5$ and a contact angle of $\vartheta = 90°$, while the mean contact angle is $\langle\vartheta\rangle_N = 71°$. These super-droplet shapes represent parts of the growth dynamics, where coalescence of droplets reduces the contact angle of the resulting droplet, which then gradually increases again with subsequent growth through additional condensation.

With the surface tension σ, both the Bond number

$$Bo = \frac{\rho_l g R_{max}}{\sigma} = 0.42 \tag{24}$$

and the Weber number

$$We = \frac{\rho u_b^2 R_{max}}{\sigma} = 0.007 \tag{25}$$

are small, and deviations from the spherical shape due to the influence of gravity and the drag of the impinging flow are neglected.

The super-droplets are included in the simulation as static deformations of the cooled channel wall. To ensure that the droplet surfaces are resolved by at least six grid points along the streamwise and spanwise directions to adequately capture their curvature, the mesh in the investigation region is refined in the streamwise direction, with $\Delta x^+ = \Delta z^+ = 3$. At the boundary of the generation domain, the grid spacing is matched to the investigation domain, but a hyperbolic tangent distribution is applied in the streamwise direction to reduce the number of cells in the precursor by 36% compared to a uniform, overresolved mesh. As a result, the resolution varies between $\Delta x^+ = 3$ at the cyclic boundaries and $\Delta x^+ = 6$ in the center. In total, the refined mesh consists of $(360 + 840) \times 162 \times 280$ cells over both domains.

To preserve the integrity and quality of the mesh, the deformation at the wall surface is transferred into the volume. The shift of each volume grid point based on the surface deformation is weighted using the Wendland function W2,

$$\mathrm{W2}(r) = \begin{cases} |r - r_{rbf}| \left(1 - \frac{r}{r_{rbf}}\right)^4 \left(1 + 4\frac{r}{r_{rbf}}\right), & r \le r_{rbf}, \\ 0 \quad \text{else}, \end{cases} \tag{26}$$

with base radius $r^+_{rbf} = 65$ as a radial base function. Solving a density matrix equation for the influence of multiple surface deformations per grid point inside the volume ensures a smooth adaptation of the entire mesh to the new surface (Köthe et al., 2014), minimizing the additional discretization error introduced by non-uniform mesh spacing.

The simulation is then run with the deformed wall as a new boundary condition until a statistically steady state is reached again, after which statistical data on the flow fields and their fluctuations are collected until fully converged.

4. Local modifications of the flow fields around super-droplets

Examination of the flow fields in the presence of the super-droplet pattern reveals the potentially large influence of sessile condensate droplets on the turbulent flow and on the continued condensation process.

Figure 5 shows the direct interaction between the super-droplets and the instantaneous streamwise velocity at two selected locations along the channel. The top panel shows the situation near the channel inlet, where the flow from the smooth precursor domain first encounters the cooled and deformed wall. The super-droplets strongly modify the previously undisturbed flow, with separation visible at the crests and recirculation of the fluid in the wake region.

Further along the channel, the changes in the flow caused by the large number of droplets upstream reduce the immediate effect of additional droplets downstream. The fluid flows around the droplets, but there is no separation or recirculation.

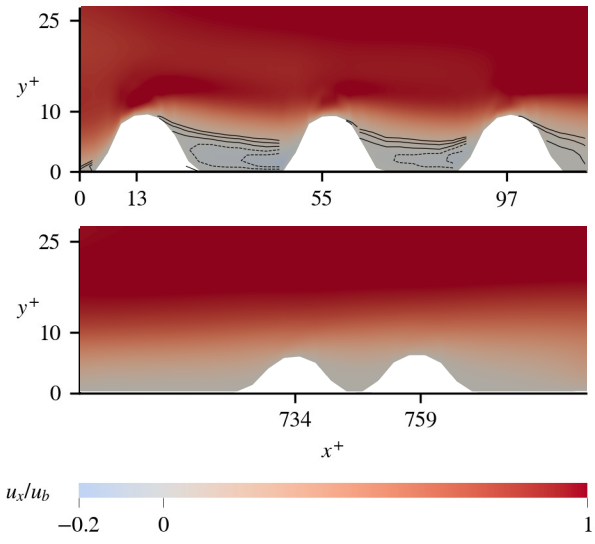

Figure 5: Top panel: The instantaneous streamwise velocity in a z-normal plane through super-droplets near the channel inlet shows separation and recirculation. The contours in the relevant regions are spaced by 0.05 for u_x between −0.1 and 0.1.
Bottom panel: Further downstream, the modifications of the flow by the upstream super-droplets reduce the direct influence of the super-droplets on the instantaneous velocity.

Taking advantage of the large number of super-droplets present in the simulation, averaging equivalent points on or near the deformation over the ensemble of all super-droplets allows the investigation of the average effect on the flow. In the neighborhood of a super-droplet i, its footprint radius R_i and the droplet height h_i are the characteristic length scales in the $x-z$ plane and in the wall-normal y direction, respectively. To identify equivalent points between different droplets, droplet-specific cylindrical coordinates are defined, using the radial distance r in the $x-z$ plane from the droplet center normalized with R_i, the height y above the undisturbed surface normalized with h_i, and the angle φ with respect to the mean flow direction along the channel axis. Points with the same coordinates are then comparable between all super-droplets. The average of a variable over the ensemble of N super-droplets on top of the temporal average is denoted by $\langle\cdot\rangle_N$ in the following.

Figure 6 shows the ensemble averages of the streamwise ($\langle u_x\rangle_N$) and wall-normal ($\langle u_y\rangle_N$) velocity components in the $x-y$ plane centered on the super-droplet. The deflection of the flow around the super-droplet is clearly visible. The fluid impinges on the upstream flank of the super-droplet, inducing a strong updraft near the crest. The recirculation found in the instantaneous velocity behind the super-droplets near the inlet does not persist in the combined average over time and super-droplet ensemble. The influence of the super-droplet extends into the volume, with modifications of the flow contours visible beyond twice the normalized height y/h. Measured at the downstream edge of the super-droplet footprint, the integrated deficit up to $y^+ = 15$ in the average streamwise flow velocity is 2.3%, with a peak deficit of 6.4% at a height of $y = 1.06h$.

In addition to the mean velocity field, the ensemble-averaged root-mean-square (rms) fluctuations of the streamwise ($\langle u_x^{rms}\rangle_N$) and wall-normal ($\langle u_y^{rms}\rangle_N$) velocity components in Figure 7 show strong fluctuations in the wall-normal component at upper part of the upstream flank of the super-droplet, where the deformation starts to emerge from the viscous sublayer and interacts with the turbulent flow through the channel. In contrast, both the streamwise and wall-normal velocity fluctuations are reduced in the droplet wake, where the obstruction by the droplet provides a degree of isolation of downstream region from the flow. This is consistent with the observation of the mean velocity deficit discussed above.

The changes in the convective heat and vapor transport caused by the deflection of the flow around the super-droplets and the interaction with the turbulence in turn affect the temperature and vapor concentration fields around the super-droplets. Figure 8 shows the ensemble-averaged dimensionless temperature and vapor, where

$$\theta = \frac{T - T_c}{\Delta T}, \tag{27}$$

defined analogously to the dimensionless vapor concentration in eq. (23). In the droplet wake, the warm and humid fluid is depleted compared to the upstream side, mirroring the deficit in the streamwise velocity. The cooling and drying of the fluid at the super-droplet surface, combined with the deflection of the flow around the super-droplet, impedes the transport of heat

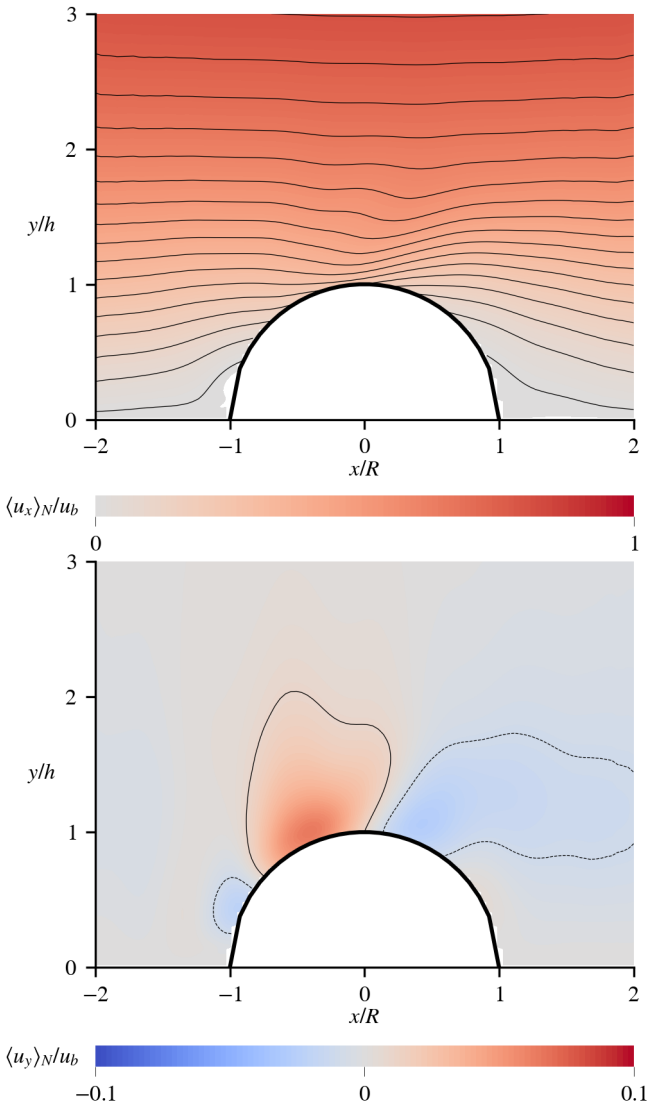

Figure 6: The ensemble-averaged streamwise (top) and wall-normal velocity (bottom) around the super-droplet, normalized with the bulk velocity u_b. Note the strong upward deflection just before the droplet crest and the streamwise velocity deficit in the droplet wake. The contours are spaced by 0.05 for $\langle u_x\rangle_N$, and at ±0.01 for $\langle u_y\rangle_N$.

and vapor from the bulk to the wake region. As with the velocity fields, the influence of the super-droplet on the scalar fields extends beyond the height of the deformation and is still visible up to $y \simeq 2h$. Steep temperature and humidity gradients at the upstream flank up to the droplet crest coincide with the location of strong fluctuations in the wall-normal velocity seen in Figure 7. Increased turbulent mixing in this region causes strong vapor and heat transport towards the droplet surface.

The turbulent transport of the scalar fields is particularly important for the influence of the super-droplets on further condensation. Showing the ensemble average of the turbulent Nusselt number in the wall-normal direction (Kuerten et al., 2011),

$$Nu_{t,y} = -\frac{\delta}{\kappa}\left\langle u_y'\theta'\right\rangle, \tag{28}$$

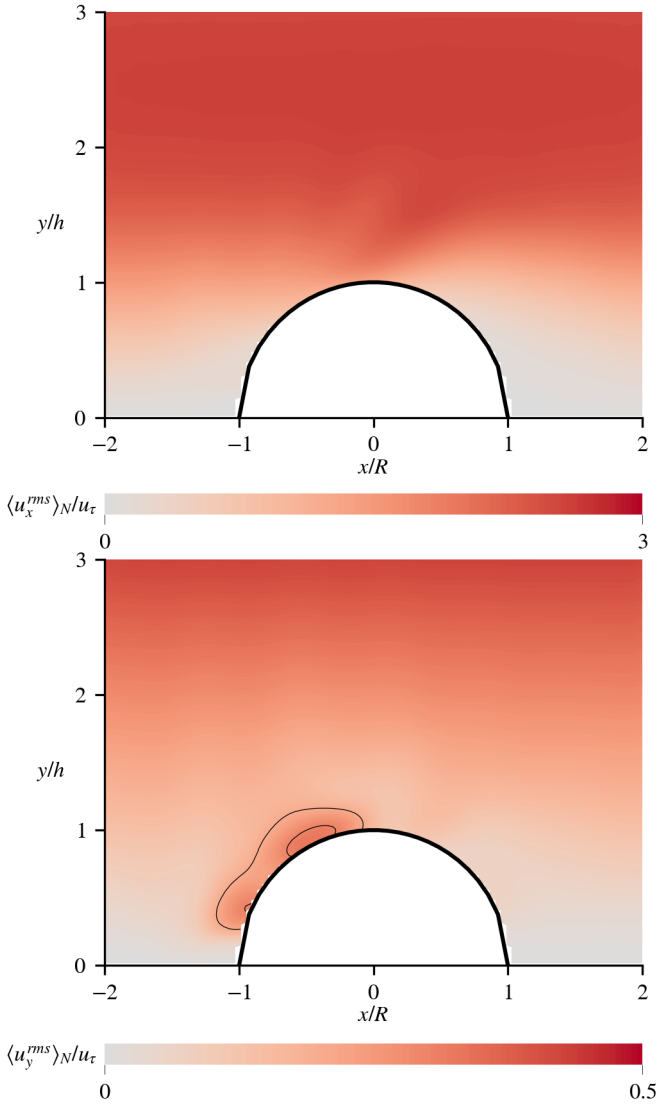

Figure 7: The ensemble-averaged fluctuations of the streamwise (top) and wall-normal velocity components (bottom) around the super-droplet, normalized with the friction velocity u_τ. Of particular note is the region of strong u_y-fluctuations on the upstream flank of the super-droplet.

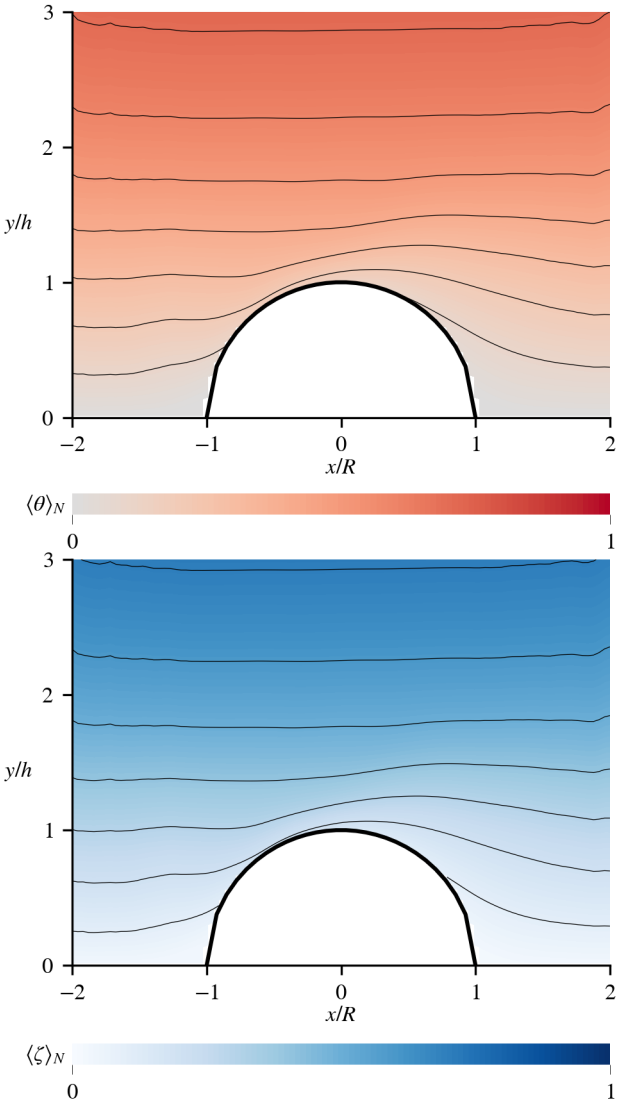

Figure 8: The ensemble-averaged dimensionless temperature (top) and vapor concentration (bottom) around the super-droplet. The deformation of the field above the droplets and the depletion of heat and humidity in the droplet wake are visible in the contours, spaced in intervals of 0.1.

with the fluctuations of the velocity u' and temperature θ' as well as the similarly defined Sherwood number,

$$Sh_{t,y} = -\frac{\delta}{D} \left\langle u_y' \zeta' \right\rangle, \tag{29}$$

in Figure 9 illustrates the change of the turbulent transport due to the super-droplets. Since the Prandtl and Schmidt numbers are similar, and both temperature and concentration experience the same convection, the distribution of the Nusselt and Sherwood numbers around the super-droplets mirror each other. Again, the region directly at the upstream flank of the super-droplet exhibits the largest effect, indicating a strong correlation between fluid flow towards the droplet and negative concentration fluctuations due to surface condensation. As warm and humid fluid originating from the bulk flows towards the droplet in turbulent sweeps, it is loses heat in the interaction with the surface, and, as the temperature drops below the dew point, simultaneously transfers vapor across the phase boundary during condensation. Critically, much less turbulent heat and vapor transfer occurs in the region surrounding the super-droplet.

This increased vapor transport rate directly affects the condensation rate at the cooled wall. Figure 10 shows a top-down view of ensemble-averaged dimensionless condensation rate $\langle \Delta\zeta_{PT} \rangle_N$ at the wall, compared between the baseline simulation without droplets on the left and with the deformed wall on the right. Despite the overall inhomogeneity of the condensation rate over the entire channel wall, the condensation rates on the smooth wall are uniform on length scales comparable to the super-droplet radius. In the presence of condensate droplets, however, the symmetry of the cooled wall is broken, and con-

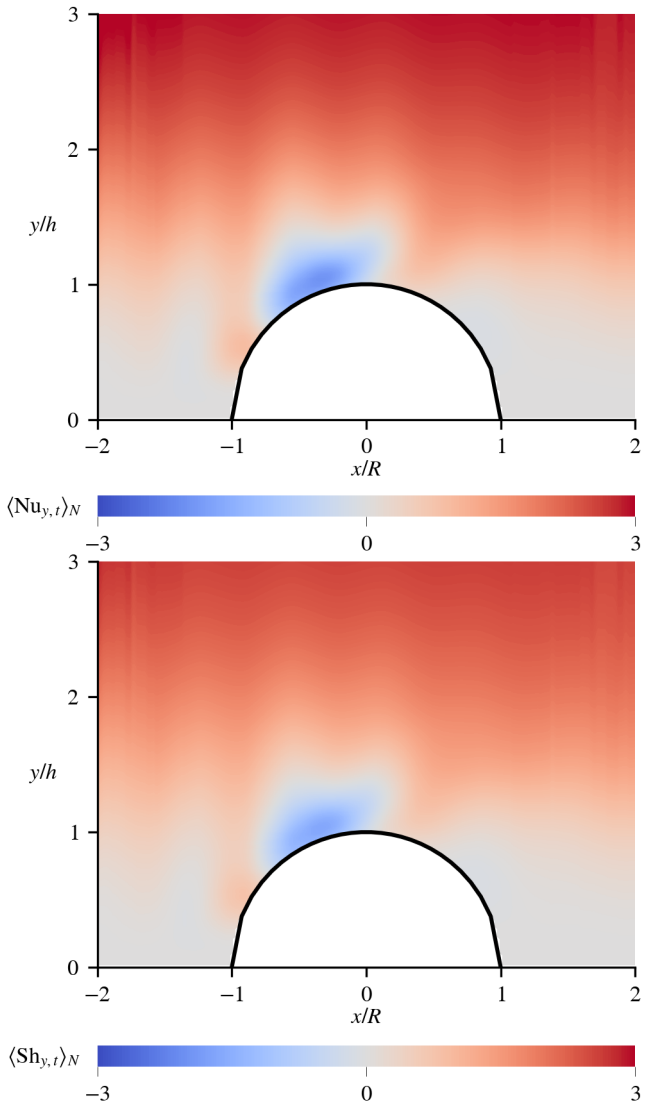

Figure 9: The wall-normal turbulent transport as quantified by the ensemble-averaged turbulent Nusselt number for the heat transport (top) and the Sherwood number for vapor transport (bottom). Both quantities behave similarly, again showing strong transport processes directly at the upstream flank of the super-droplet.

densation is focused on the surface of the super-droplets, shifted away from the surrounding smooth surface, where condensation rates are reduced in comparison. In fact, the region with the highest condensation rates is the upstream flank of the super-droplet, extending up to the crest. This corresponds exactly to the region of increased wall-normal velocity fluctuations and increased vapor transport discussed above in Figure 9, confirming the conclusion that here, scalar transport towards the super-droplet is significantly enhanced by the influence of the wall deformation on the turbulent flow.

Along the entire channel, the modifications of the turbulent heat and mass transfer around the super-droplets change the overall pattern of the wall-normal transport. The presence of the surface deformations breaks the symmetry of the wall and

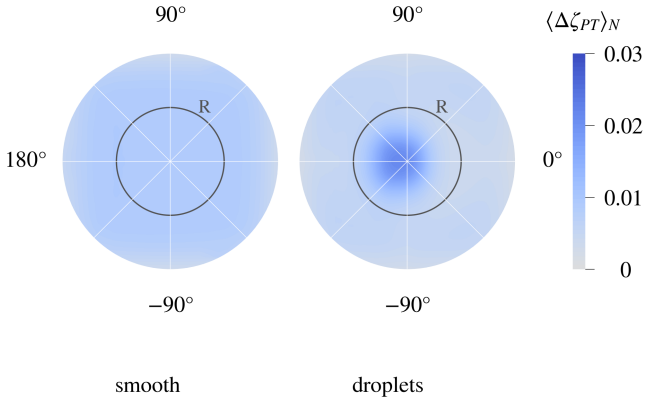

Figure 10: The distribution of the ensemble-averaged condensation rate over the super-droplet (enclosed by its perimeter with radius R) and the surrounding region, shown on the right, compared to the equivalent region in the simulation with a smooth wall on the left.

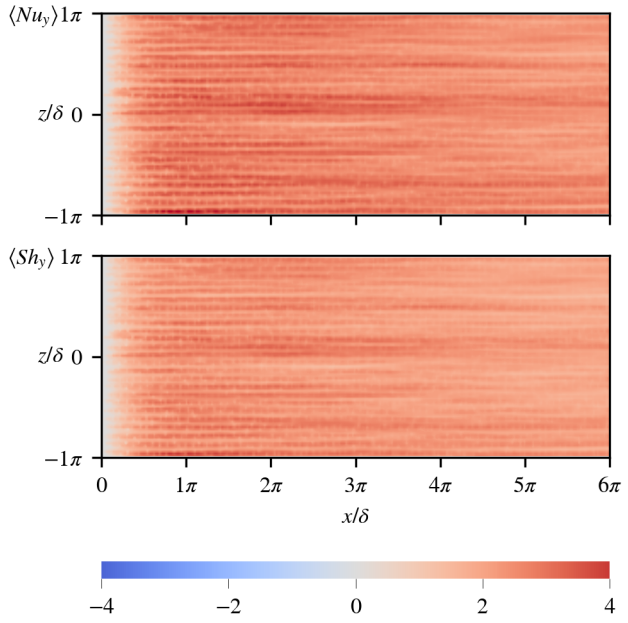

Figure 11: The Nusselt number (top) and Sherwood number (bottom) in a wall-parallel plane at $y^+ = 15$ shows the increased wall-normal heat and mass transfer above the super-droplets. The added variation in $\langle Nu_y \rangle$ and $\langle Sh_y \rangle$ from the droplet effect is visible on top of the spanwise variation caused by the underlying streaky structure of the turbulent flow.

introduces regions which strongly favor condensation over the surrounding areas. Figure 11 shows the time-averaged Nusselt and Sherwood numbers in a wall-parallel plane at $y^+ = 15$. The influence of the super-droplet pattern is clearly visible in the plane passing over the top of the droplets, showing a significant increase of turbulent transport of warm and humid fluid towards the wall at the super-droplets. Again, both heat and mass transfer exhibit very similar behavior to each other.

This enhanced and modified wall-normal transport results in a markedly different distribution of the condensation rate compared to the smooth wall in Figure 3. Figure 12 shows the result

for the simulation with super-droplets at the wall.

In addition to the inhomogeneity introduced by the super-droplets, the variations in condensation rate along the channel observed with the smooth wall, with higher rates near the inlet and spanwise variations, are still present. These result from features of the overall flow, with the available vapor decreasing further along the channel and the spanwise structures found in the flow unaffected by the surface modifications (Grass, 1971).

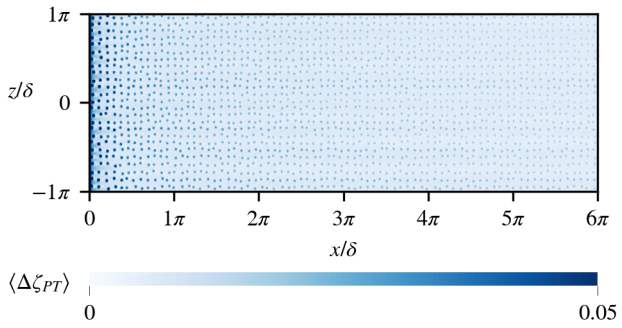

Figure 12: The distribution of the average condensation rate at the cooled wall with sessile super-droplets. Condensation is strongly focused on the droplets, while the streamwise and spanwise variability of the smooth case persists.

Condensation that preferentially occurs on the surface of existing super-droplets mirrors the thermodynamic phenomenon of Ostwald ripening (Madras and McCoy, 2001), where larger droplets experience more additional condensation than smaller droplets due to the difference in surface energy of the curved interface. Since this thermodynamic effect is not included in the simulation, the observation of similar behavior reveals an analogous effect resulting from the interaction between turbulent flow and the droplet geometry alone.

5. Global heat and mass transfer modifications

The simulation approach focusing only on the gas phase and modeling the condensate droplets as static wall deformations allows the investigation of the effect of condensation over the entire length of the channel. Following from the effect of the super-droplets on the transport processes at the wall, the macroscopic evolution of both scalar fields is affected by the added condensate droplets. Considering both temperature and vapor concentration in terms of the associated thermal energy flux along the streamwise direction allows a combined discussion of both quantities. The sensitive heat flux is

$$\phi_s = \langle\theta\rangle_b \Delta T \rho c_p u_b, \tag{30}$$

with the bulk-averaged dimensionless temperature

$$\langle\theta\rangle_b = \frac{\int \theta \mathbf{u} \cdot \mathrm{d}\mathbf{A}}{\int \mathbf{u} \cdot \mathrm{d}\mathbf{A}}, \tag{31}$$

where A is the cross-sectional area of the channel. Similarly, the latent heat flux is then given by

$$\phi_l = \langle\zeta\rangle_b \Delta c \rho_v h u_b, \tag{32}$$

with the bulk-averaged dimensionless concentration defined analogously to eq. (31).

Adding both contributions and normalizing with the total flux at the channel inlet $\phi_s^{in} + \phi_l^{in}$ gives

$$\phi = \frac{\phi_s + \phi_l}{\phi_s^{in} + \phi_l^{in}} = \frac{\langle\theta\rangle_b + (\tilde{\rho}/Ja)\,\langle\zeta\rangle_b}{1 + (\tilde{\rho}/Ja)}, \tag{33}$$

the total remaining heat flux at position x along the channel, with the density ratio $\tilde{\rho} = \Delta c \rho_v / \rho$ between the effective vapor density and the density of the fluid as a whole. Figure 13 shows the progression of ϕ compared for the simulations with and without super-droplets. The deficit in heat flux through the channel cross section compared to the inlet is equal to the accumulated flux through the cooled wall. Along the entire channel, more thermal energy is removed through the droplet-covered wall than through the smooth wall. At the outlet, the accumulated deficit amounts to $\Delta\phi = 0.050$ without super-droplets and $\Delta\phi = 0.055$ with super-droplets, for an increase of 10%. Critically, this is greater than the increase in wall area of 6.4% from the curved droplet surfaces, confirming additional energy transfer due to changes in the turbulent flow.

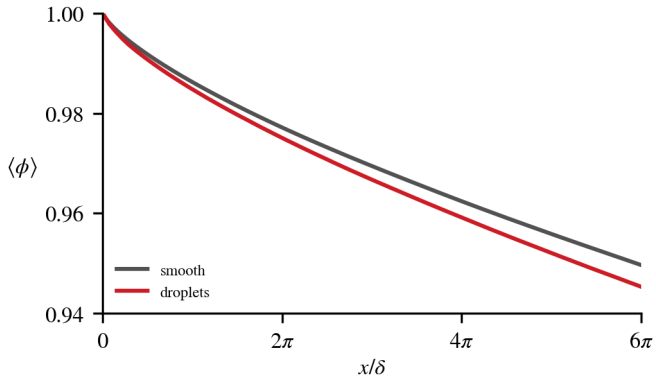

Figure 13: Evolution of the normalized total amount of thermal energy flux along the channel. The presence of super-droplets significantly increases the energy transfer at the cooled wall, resulting in a larger deficit at the outlet.

To compensate for the additional thermal energy removed from the channel at the wall in the presence of droplets, the transport of heat and vapor inside the channel towards the wall must be increased accordingly. The modification of the turbulent transport on the scale of the whole channel is the continuation of the modified flow fields in the immediate vicinity of the super-droplets. In addition to the temporal averaging, the quantities are averaged over the spanwise coordinate z, denoted by $\langle\cdot\rangle_z$ Figure 14 shows wall-normal profiles of the rms-fluctuations of the streamwise and wall-normal components of the velocity at the channel outlet. Here, the accumulated effects of condensation and the super-droplets are greatest, as the flow has been subject to their influence for the entire residence time of the fluid in the channel. Both velocity components show increased fluctuations in the case with super-droplets caused by the deflection of the flow around the individual droplets, as shown above in Figures 6 and 7. This combines with the op-

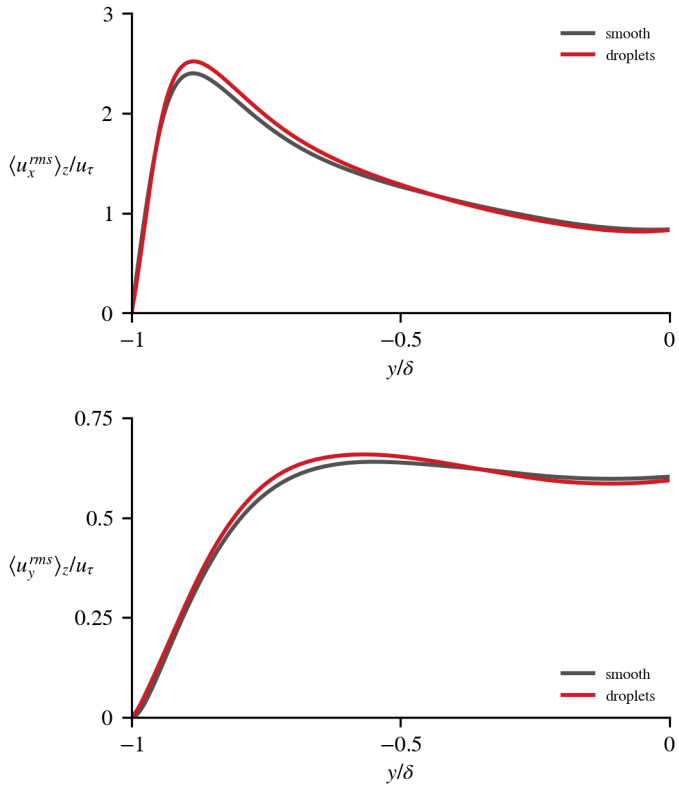

Figure 14: Streamwise (top) and wall-normal velocity fluctuations compared between simulations with and without super-droplets.

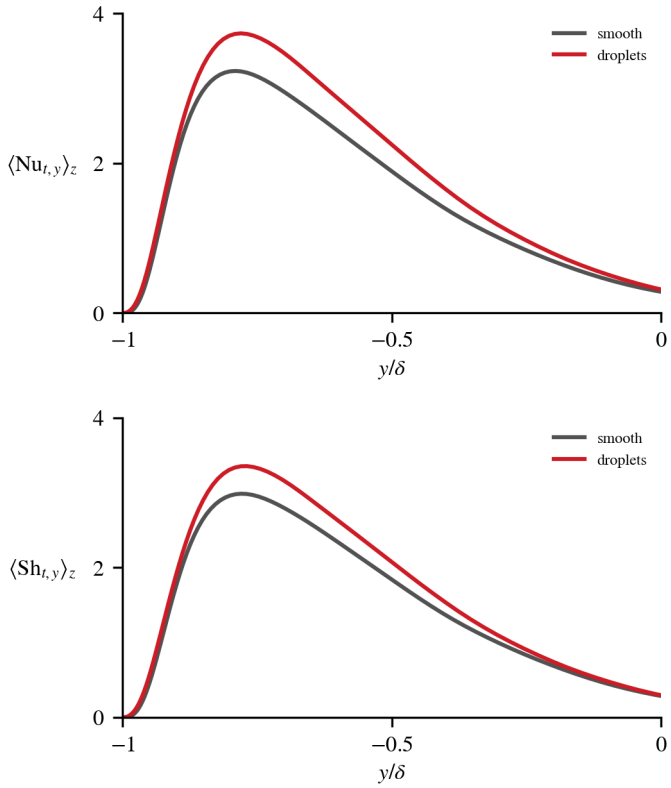

Figure 15: Comparison of the turbulent Nusselt (top) and Sherwood numbers (bottom) with and without super-droplets at the cooled wall, averaged in time and along the spanwise direction.

posing buoyancy resulting from the release of latent heat during condensation, which acts against the aiding buoyant force due to the cooling at the wall. The overall reduction in the effectiveness of the aiding buoyancy as a result of condensation limits its damping effect (Kasagi and Nishimura, 1997; Wetzel and Wagner, 2019), thereby increasing the turbulence near the cooled wall.

Increased mixing due to changes to the velocity field then affects the turbulent transport of heat and vapor in the wall-normal direction. Higher turbulence intensity leads to more transfer of warm and humid fluid in sweeps, moving from the bulk towards the cooled wall. Figure 15 shows the marked change of the dimensionless heat and mass transfer in terms of the Nusselt and Sherwood numbers in the simulation with super-droplets, with peaks increasing by 15.8% and 12.4%, respectively.

6. Conclusions

For the range of temperatures and humidity typically encountered at ambient conditions and therefore relevant to ventilation applications, condensation on cooled surfaces dominates over droplet formation within the flow volume. Under these circumstances, the combination of neglecting the dispersed liquid phase within the volume and modeling the sessile condensate droplets at the wall as static deformations based on agglomerated super-droplets allows DNS of flows with phase transition while incurring none of the computational costs associated with multiphase DNS techniques.

Due to the slow growth dynamics of droplets at the condensation rates found at ambient conditions, super-droplets act as static obstacles with respect to the turbulent flow. While the separation of flow and droplet time scales precludes fully resolved simulations of the growth of super-droplet patterns, the single-phase approach uses the average condensation rates obtained over a time interval on the scale of the convective time scale to extrapolate the accumulation of condensate mass over the much longer time scales of droplet growth, taking advantage of the large difference between the two scales.

The pattern of synthetic super-droplets preserves the underlying inhomogeneity of the condensation rates, while at the same time simplifying the droplet distribution by creating one representative droplet per grid cell, thereby collecting all locally available condensate mass.

Investigation of the effects of the droplet pattern on the flow through the channel shows that large sessile condensate droplets on the wall surface are an important aspect of flows with condensation at ambient conditions, as relevant for ventilation applications. Their presence significantly alters the flow in the sensitive wall-near region, and the interactions with the turbulent flow project the influence of the super-droplets outwards towards the bulk. In particular, the increase in turbulent mixing leads to an increase in the turbulent transport of heat and mass

towards the cooled surface. Here, the breaking of the uniformity of the wall concentrates further condensation on the surface of existing super-droplets in a positive feed-back effect.

The inclusion of static, sessile condensate super-droplets extends the previously established single-phase approach to DNS of flows with surface condensation to include the significant contributions of the condensate to the overall effect of condensation on the flow and the transport of heat and mass. The flexibility of the approach as presented here allows for refinement to include additional aspects of dropwise condensation, such as constraining the super-droplet pattern to not only conserve mass locally, but to respect a global size distribution, or modifying the saturation pressure at curved interfaces, without compromising the computational cost advantages inherent in the method.

References

Alduchov, O.A., Eskridge, R.E., 1996. Improved magnus form approximation of saturation vapor pressure. Journal of Applied Meteorology 35, 601–609. doi:10.1175/1520-0450(1996)035¡0601:imfaos¿2.0.co;2.

Bahavar, P., Wagner, C., 2020. Condensation-induced flow structure modifications in turbulent channel flow investigated in direct numerical simulations. Physics of Fluids 32, 015115. doi:10.1063/1.5128976.

Balachandar, S., Eaton, J.K., 2010. Turbulent dispersed multiphase flow. Annual Review of Fluid Mechanics 42, 111–133. doi:10.1146/annurev.fluid.010908.165243.

Bellec, M., Toutant, A., Olalde, G., 2017. Large eddy simulations of thermal boundary layer developments in a turbulent channel flow under asymmetrical heating. Computers and Fluids 151, 159–176. doi:10.1016/j.compfluid.2016.07.001.

Chan-Braun, C., Garcia-Villalba, M., Uhlmann, M., 2011. Force and torque acting on particles in a transitionally rough open-channel flow. Journal of Fluid Mechanics 684, 441–474. doi:10.1017/jfm.2011.311.

Chorin, A.J., 1968. Numerical solution of the navier–stokes equations. Mathematics of Computation 22, 745–745. doi:10.1090/S0025-5718-1968-0242392-2.

Grass, A.J., 1971. Structural features of turbulent flow over smooth and rough boundaries. Journal of Fluid Mechanics 50, 233–255. doi:10.1017/s0022112071002556.

Gray, D.D., Giorgini, A., 1976. The validity of the boussinesq approximation for liquids and gases. International Journal of Heat and Mass Transfer 19, 545 – 551. doi:10.1016/0017-9310(76)90168-X.

Hammou, Z.A., Benhamou, B., Galanis, N., Orfi, J., 2004. Laminar mixed convection of humid air in a vertical channel with evaporation or condensation at the wall. International Journal of Thermal Sciences 43, 531–539. doi:10.1016/j.ijthermalsci.2003.10.010.

Issa, R., 1986. Solution of the implicitly discretised fluid flow equations by operator-splitting. Journal of Computational Physics 62, 40–65. doi:10.1016/0021-9991(86)90099-9.

Jiménez, J., Moin, P., 1991. The minimal flow unit in near-wall turbulence. Journal of Fluid Mechanics 225, 213–240. doi:10.1017/S0022112091002033.

Kasagi, N., Nishimura, M., 1997. Direct numerical simulation of combined forced and natural turbulent convection in a vertical plane channel. International Journal of Heat and Fluid Flow 18, 88–99. doi:10.1016/S0142-727X(96)00148-8.

Kath, C., Wagner, C., 2016. Highly resolved simulations of turbulent mixed convection in a vertical plane channel, in: Notes on Numerical Fluid Mechanics and Multidisciplinary Design. Springer International Publishing, pp. 515–524. doi:10.1007/978-3-319-27279-5_45.

Kim, S., Kim, K.J., 2011. Dropwise condensation modeling suitable for superhydrophobic surfaces. Journal of Heat Transfer 133. doi:10.1115/1.4003742.

Kuerten, J.G.M., 2016. Point-particle DNS and LES of particle-laden turbulent flow - a state-of-the-art review. Flow, Turbulence and Combustion 97, 689–713. doi:10.1007/s10494-016-9765-y.

Kuerten, J.G.M., van der Geld, C.W.M., Geurts, B.J., 2011. Turbulence modification and heat transfer enhancement by inertial particles in turbulent channel flow. Physics of Fluids 23, 123301. doi:10.1063/1.3663308.

Köthe, T., Herzog, S., Wagner, C., 2014. Shape optimization of aircraft cabin ventilation components using adjoint CFD, in: Engineering Optimization 2014, CRC Press. pp. 675–680. doi:10.1201/b17488-120.

Leriche, M., Roessner, W., Reister, H., Weigand, B., 2015. Numerical investigation of droplets condensation on a windshield: Prediction of fogging behavior, in: SAE Technical Paper Series, SAE International. doi:10.4271/2015-01-0360.

Lorenz, M., 2015. Reduction of heating loads and interior window fogging in vehicles. Ph.D. thesis. Technische Universität München.

Madras, G., McCoy, B.J., 2001. Distribution kinetics theory of ostwald ripening. The Journal of Chemical Physics 115, 6699–6706. doi:10.1063/1.1403687.

Manhart, M., 2004. A zonal grid algorithm for DNS of turbulent boundary layers. Computers & Fluids 33, 435–461. doi:10.1016/s0045-7930(03)00061-6.

Marek, R., Straub, J., 2001. Analysis of the evaporation coeffcient and the condensation coeffcient of water. International Journal of Heat and Mass Transfer 44, 39–53. doi:10.1016/S0017-9310(00)00086-7.

Medici, M.G., Mongruel, A., Royon, L., Beysens, D., 2014. Edge effects on water droplet condensation. Phys. Rev. E 90, 062403. doi:10.1103/PhysRevE.90.062403.

Niu, D., Tang, G., 2018. Molecular dynamics simulation of droplet nucleation and growth on a rough surface: revealing the microscopic mechanism of the flooding mode. RSC Advances 8, 24517–24524. doi:10.1039/c8ra04003f.

Orazzo, A., Tanguy, S., 2019. Direct numerical simulations of droplet condensation. International Journal of Heat and Mass Transfer 129, 432–448. doi:10.1016/j.ijheatmasstransfer.2018.07.094.

Rose, J.W., 2002. Dropwise condensation theory and experiment: A review. Proceedings of the Institution of Mechanical Engineers, Part A: Journal of Power and Energy 216, 115–128. doi:10.1243/09576500260049034.

Russo, E., Kuerten, J.G.M., van der Geld, C.W.M., Geurts, B.J., 2014. Water droplet condensation and evaporation in turbulent channel flow. Journal of Fluid Mechanics 749, 666–700. doi:10.1017/jfm.2014.239.

Shima, S., Kusano, K., Kawano, A., Sugiyama, T., Kawahara, S., 2009. The super-droplet method for the numerical simulation of clouds and precipitation: a particle-based and probabilistic microphysics model coupled with a non-hydrostatic model. Quarterly Journal of the Royal Meteorological Society 135, 1307–1320. doi:10.1002/qj.441.

Shishkina, O., Wagner, C., 2004. Stability conditions for the leapfrog-euler scheme with central spatial discretization of any order. Applied Numerical Analysis & Computational Mathematics 1, 315–326. doi:10.1002/anac.200310028.

Témam, R., 1969. Sur l'approximation de la solution des équations de navier-stokes par la méthode des pas fractionnaires (II). Archive for Rational Mechanics and Analysis 33, 377–385. doi:10.1007/bf00247696.

The OpenFOAM Foundation, . www.openfoam.org. URL: `www.openfoam.org`.

Tryggvason, G., Esmaeeli, A., Al-Rawahi, N., 2005. Direct numerical simulations of flows with phase change. Computers & Structures 83, 445–453. doi:10.1016/j.compstruc.2004.05.021.

Wagner, C., 1996. Direkte numerische Simulation turbulenter Strömungen in einer Rohrerweiterung. VDI-Verlag, Düsseldorf.

Wetzel, T., Wagner, C., 2019. Buoyancy-induced effects on large-scale motions in differentially heated vertical channel flows studied in direct numerical simulations. International Journal of Heat and Fluid Flow 75, 14–26. doi:10.1016/j.ijheatfluidflow.2018.09.005.